Necking of the Lithosphere: A Reappraisal of Basic Concepts With Thermo-Mechanical Numerical Modeling

Pauline Chenin, Stefan Markus Schmalholz, Gianreto Manatschal, Garry D. Karner

AGU100 ADVANCING EARTH AND SPACE SCIENCE

JGR

Journal of Geophysical Research: Solid Earth

RESEARCH ARTICLE
10.1029/2017JB014155

Key Points:
- Modeled and natural necking zones widths are consistent without need for strain softening or weakening mechanisms
- Boundary conditions type and initial Moho wavelength do not impact modeled necking zones width
- Asynchronous and depth-dependent crust/mantle necking results in a complex surface topography evolution

Correspondence to:
P. Chenin,
pauline.chenin@fulbrightmail.org

Citation:
Chenin, P., Schmalholz, S. M., Manatschal, G., & Karner, G. D. (2018). Necking of the lithosphere: A reappraisal of basic concepts with thermo-mechanical numerical modeling. *Journal of Geophysical Research: Solid Earth*, *123*, 5279–5299. https://doi.org/10.1029/2017JB014155

Received 1 MAR 2017
Accepted 18 MAY 2018
Accepted article online 24 MAY 2018
Published online 22 JUN 2018

Necking of the Lithosphere: A Reappraisal of Basic Concepts With Thermo-Mechanical Numerical Modeling

Pauline Chenin[1], Stefan M. Schmalholz[2], Gianreto Manatschal[1], and Garry D. Karner[3]

[1]Centre National de la Recherche Scientifique-Institut de Physique du Globe de Strasbourg, Université de Strasbourg, Strasbourg, France, [2]Institut des Sciences de la Terre, Université de Lausanne, Lausanne, Switzerland, [3]Global Tectonics & Structure, ExxonMobil Exploration Company, Houston, Texas, USA

Abstract We investigate lithosphere necking using two-dimensional thermo-mechanical numerical simulations without strain softening or weakening mechanisms. The models have an initial small sinusoidal perturbation of the Moho depth, whose wavelength corresponds to the model width. Applied boundary conditions (constant extension velocity or bulk extension rate) and initial model width significantly impact the necking dynamics. For constant bulk extension rates, wider models generate more intense necking with locally higher strain rates, whereas for constant velocity extension, models evolution is similar independent on their initial width. However, the width of the final necking zones ranges consistently between 45 and 105 km, independent on the type of applied boundary conditions and the initial Moho wavelength. The modeled widths are similar to along dip necking zones widths of natural rifted margins that formed during a single, unidirectional, and relatively continuous extensional event (e.g., Iberia-Newfoundland margins, Porcupine Basin, Gulf of Aden). When the crust is mechanically decoupled from the mantle by a weak ductile lower crust, models exhibit three characteristic stages: (1) distributed thinning and extension associated with progressive subsidence; (2) upper mantle necking compensated by flow of the weak lower crust, which hampers both crustal thinning and subsidence at the rift center; and (3) crustal necking associated with fast subsidence after the mantle has necked. Decoupled models display regions of relatively thick crust on one or both sides of the rift center, comparable to the Galicia, Rockall, Hatton, and Porcupine Banks along the North Atlantic rifted margins.

1. Introduction

At rifted continental margins, the so-called necking zone or necking domain (in the sense of Sutra et al., 2013; Figure 1a) corresponds to the region where the crust thins abruptly from ~30–35 to ~10 km. Significant crustal thinning in this domain, referred to as *crustal necking*, is likely a consequence of attenuating ductile layers (e.g., Pérez-Gussinyé & Reston, 2001). This phase of necking usually follows a phase of distributed extension that does not generate significant crustal thinning and forms the so-called proximal domain (e.g., Sutra et al., 2013). The necking phase ends with the full embrittlement of the continental crust, which corresponds to the onset of hyperextension and subsequent formation of the *hyperextended domain* (e.g., Nirrengarten et al., 2016). The transition between the proximal and the necking domain, as well as the transition between the necking and hyperextended domain, are highlighted by changes in the dip of both the top basement and the crust-mantle boundary (red lines on Figure 1a).

According to the compilation of rift domains measurements by Chenin et al. (2017), the width of necking zones in natural rift systems ranges from 10 to 100 km. Recently, Schmalholz and Mancktelow (2016) showed that the application of the analytical solution of Fletcher and Hallet (1983) to crustal necking predicts a comparable range of widths for necking zones (14–83 km) and thus argued that the formation of crustal necking zones may be primarily controlled by a viscoplastic necking instability (see Appendix A2). A goal of this study is to compare the width of necking zones from natural rift systems with both necking zones widths predicted by analytical studies and formed in thermo-mechanical numerical simulations of lithosphere extension.

Extension and rifting of the lithosphere have been extensively modeled using thermo-mechanical numerical simulations during the past 30 years (e.g., Bassi, 1991; Brune & Autin, 2013; Buck, 1991; Huismans et al., 2001; Huismans & Beaumont, 2011; Naliboff & Buiter, 2015; Rosenbaum et al., 2010), but no study focused on the details of finite amplitude necking per se. Moreover, in many models, either a weak seed or a significant local

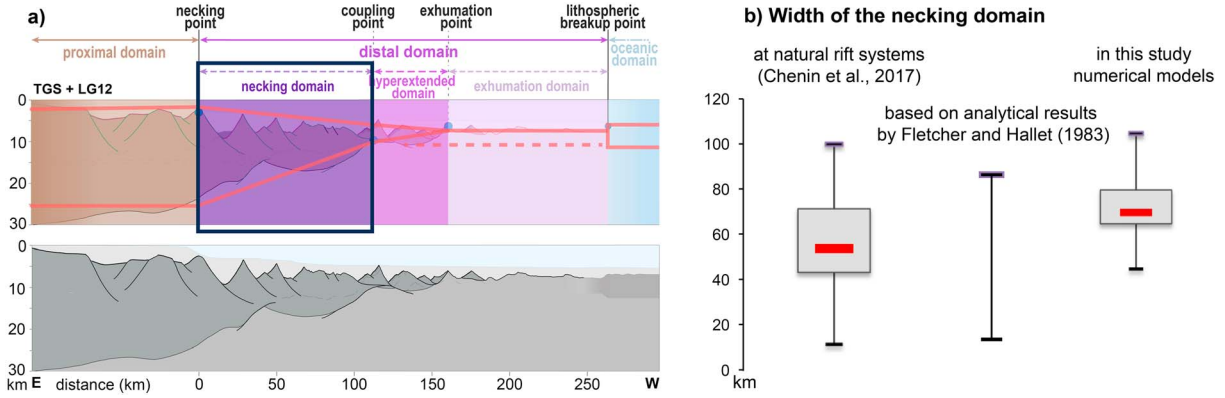

Figure 1. (a) Location and first-order morphology (red lines) of the necking domain at natural rifted margins (modified after Sutra et al. (2013) and Chenin et al. (2017). (b) Box plots representing the width of the necking domain: (left-hand plot) measured at natural rift systems by Chenin et al. (2017); (central plot) calculated from the analytical study by Fletcher and Hallet (1983; see Appendix A2); and (right-hand plot) measured at the final stage of 30 numerical models produced in this study.

thermal anomaly is introduced to force the localization of deformation and thinning. In such models necking is strongly prescribed by these initial heterogeneities (Dyksterhuis et al., 2007).

In this contribution, we use two-dimensional thermo-mechanical numerical modeling to study lithospheric, and more specifically crustal necking processes and their structural consequences. We follow the main objectives of analytical studies, that is using simple models and focussing on first-order processes. Nevertheless, we integrate some of the geological complexity by considering the dependency of rock viscosity and density on temperature, dislocation creep flow laws, and energy conservation (i.e., the conversion of dissipative work into heat, so-called shear heating). The applied thermo-mechanical models are more complex than the analytical models but still considerably simplified because we consider, for example, a homogeneous crust and mantle, ignore material softening mechanisms such as grain size reduction and strain softening (see Appendix A1) and neglect the role of fluids and mineral reactions.

To better understand the formation of necking zones, we first quantify the impact of different extensional boundary conditions on necking, namely, constant bulk extensional rate versus constant extensional velocity. Testing the effect of constant velocity versus constant strain rate boundary conditions is important because analytical studies usually assume constant strain rate extension (e.g., Fletcher & Hallet, 1983; Zuber et al., 1986), while most numerical models employ constant velocity boundary conditions (e.g., Brune et al., 2014; Buck, 1991; Huismans & Beaumont, 2011). Analytical solutions are typically based on a constant bulk extension rate because necking is treated as an unstable deformation, which perturbs a basic state flow of pure shear extension and associated thinning. A constant bulk extension rate implies that the extension velocities become larger when the model becomes wider during extension because the bulk extension rate is the ratio of the absolute extension velocity at the model sides to the model width. A further boundary condition, not considered here, is extension under a constant extensional force, which causes a considerable increase of the extension velocities with progressive necking (Brune et al., 2016; Schmalholz, 2011; Schmalholz et al., 2008). A simple correlation between extension velocity/strain rate and extensional force is not trivial because the extensional force is related to the vertical integral of the yield strength envelope and this envelope can change significantly during extension. England (1983) investigated the effect of constant strain rate versus decreasing strain rate (constant velocity) extension of the lithosphere on the strength of this lithosphere. He predicted that the rift "maximum extension" is generally lower for constant velocity extension than for constant strain rate extension. However, this study was conducted for the entire rifting process and assumed extremely simplified rheologies, thus it cannot be restricted to the necking phase only. Furthermore, the effect of constant velocity versus constant strain rate boundary conditions has never been tested with recent thermo-mechanical numerical models considering different rheological stratifications of the lithosphere and their effect on the characteristics of finite amplitude necking has never been discussed before.

Second, we analyze the effect of the lithospheric rheological architecture, namely, (i) a mechanically decoupled lithosphere where the brittle-plastic upper crust and upper mantle are decoupled by a weak ductile lower crust (Figure 2a) and (ii) a coupled lithosphere comprising a strong brittle-plastic lower crust (Figure 2b).

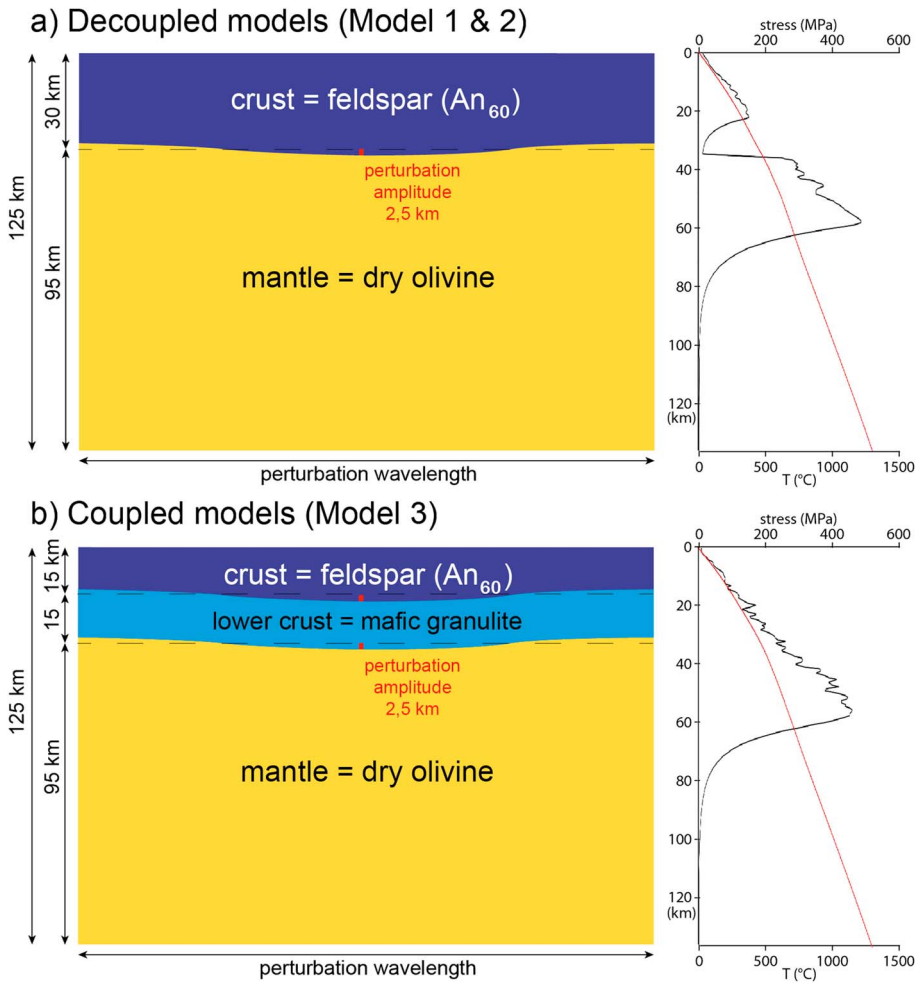

Figure 2. Architecture of the numerical models and corresponding geotherm (red line) and depth-dependent stress profile (black line) at the center of the rift. (a) Model with a ductile decoupling middle crust ("decoupled models": Models 1 and 2 and Model Series 1 and 2); (b) Model with entirely brittle crust and uppermost mantle ("coupled models": Model 3 and Model Series 3). The initial model width is 300 km for Models 1, 2, and 3. Initial model width varies between 150 and 1,200 km in Model Series 1 and 2. Extension is at a constant strain rate ($10^{-15}s^{-1}$) in Models 1 and 3 and in Model Series 1 and 3 and at constant velocity (1 cm/year full rate) in Model 2 and Model Series 2. Mass and volume are conserved during extension.

The state of mechanical coupling is of importance if we consider that the necking process is related to the attenuation of ductile material, which is commonly accepted by the scientific community (see above). Contrary to most studies, our models do not include strain softening or weakening mechanisms (see Appendix A1 for discussion), which allows us to focus on the viscoplastic necking process of a multilayer lithosphere alone. Our thermo-mechanical model configuration and model settings are somehow comparable to the "thickened crust end-member" from Huismans et al. (2001), except that our crustal thickness perturbation is much lower (2.5 km instead of 10 km) and we do not add a thermal perturbation.

Lastly, we test the influence of the initial model width/perturbation wavelength of the crust-mantle boundary on the characteristics of crustal and lithospheric necking and surface topography evolution. Instead of using geometrical perturbations as in our models, some authors impose a periodic vertical displacement at the horizontal extension boundary conditions to prevent localization of deformation at model edges without using any type of material heterogeneity (e.g., Rosenbaum et al., 2010). We prefer using a geometrical perturbation of the Moho, testing various wavelengths, because regional Moho perturbations are common on Earth as a consequence of tectonic processes such as orogeny and rifting.

2. Method

2.1. Mathematical Model

The applied 2-D force balance equation without inertia terms is

$$\frac{\partial \sigma_{ij}}{\partial x_j} = -\rho a_i \tag{1}$$

where x_i are the spatial coordinates, $a_i = [0\ g]^T$, g is the gravitational acceleration, and σ_{ij} are the components of the total stress tensor, defined as follows:

$$\sigma_{ij} = -P\delta_{ij} + \tau_{ij} \tag{2}$$

where subscripts i and j are either 1 or 2 with 1 corresponding to the horizontal and 2 to the vertical direction (repeated indices are summed), δ_{ij} is the Kronecker delta, τ_{ij} are the components of the deviatoric stress tensor and P is the pressure (or negative mean stress)

$$P = -\frac{\sigma_{11} + \sigma_{22}}{2}\,. \tag{3}$$

Incompressible flow is considered and the mass conservation equation is as follows:

$$\frac{\partial v_i}{\partial x_i} = 0 \tag{4}$$

where v_i is the component of the velocity vector.

The temperature dependence and pressure dependence of density ρ is approximated with the equation of state:

$$\rho = \rho_0(1 - \alpha T + \beta P) \tag{5}$$

where ρ_0 is the density at 0°C, α is the thermal expansion coefficient, β is the compressibility, and T is the temperature. Density variations are only considered for the evaluation of body forces under gravity (Boussinesq approximation).

The constitutive equation for all material phases describes an incompressible, viscoelastic linear Maxwell model:

$$\dot{\epsilon}_{ij} = \frac{1}{2\eta}\tau_{ij} + \frac{1}{2G}\frac{D\tau_{ij}}{Dt} = \dot{\epsilon}_{ij}^{VP} + \dot{\epsilon}_{ij}^{EL} \tag{6}$$

where $\dot{\epsilon}_{ij}$ are the components of the deviatoric strain rate tensor; superscripts VP and EL correspond, respectively, to viscoplastic (see below for plasticity implementation) and elastic fraction of the strain rate tensor; $\frac{D}{Dt}$ is the upper convective time derivative of the stress tensor (Schmalholz et al., 2001); and G is the shear modulus. Dislocation creep is considered, for which the effective viscosity η is as follows:

$$\eta = \mu \left(\frac{\dot{\epsilon}_{II}^{VP}}{\dot{\epsilon}^{BG}}\right)^{\left(\frac{1}{n}-1\right)} \exp\left[\frac{Q}{nR}\left(\frac{1}{T} - \frac{1}{T_c}\right)\right] \tag{7}$$

where Q is the activation energy, R is the gas constant, and n is the power-law stress exponent. The reference viscosity, μ, is evaluated for a reference temperature T_c (temperature at the Moho at $t = 0$) and a reference strain rate ($\dot{\epsilon}^{BG}$, here the bulk shortening strain rate) according to

$$\mu = \frac{2^{\frac{1}{n}-1}}{3^{\frac{1}{2n}+\frac{1}{2}}} A^{-\frac{1}{n}} (\dot{\epsilon}^{BG})^{\frac{1}{n}-1} \exp\left[\frac{Q}{nRT_c}\right] \tag{8}$$

with A corresponding to the pre-exponential coefficient. The second invariant of the viscoplastic part of the strain rate tensor, $\dot{\epsilon}_{II}^{VP}$, excludes elastic strain rates and is calculated as

$$\dot{\epsilon}_{II}^{VP} = \frac{\tau_{II}}{2\eta}. \tag{9}$$

The square root of the second invariant of the deviatoric stress tensor, τ_{II}, is defined as follows:

$$\tau_{II} = \sqrt{\frac{1}{2}\left(\tau_{11}^2 + \tau_{12}^2 + \tau_{21}^2 + \tau_{22}^2\right)} = \sqrt{\tau_{11}^2 + \tau_{12}^2} \tag{10}$$

assuming stress tensor symmetry ($\tau_{12} = \tau_{21}$) and the definition of the stress deviator $\tau_{11} = -\tau_{22}$.

The rheology of the mantle lithosphere is a combination of dislocation creep and Peierls creep rheology (Goetze & Evans, 1979; Molnar & Jones, 2004; Schmalholz & Fletcher, 2011) where the effective viscosity for Peierls creep is as follows:

$$\eta_P = \frac{\sigma_0}{2E\sqrt{3}}\left(1 - \sqrt{\frac{RT}{H}\ln\left(\sqrt{3}\frac{\dot{\epsilon}_0}{2E}\right)}\right) \tag{11}$$

with $\sigma_0 = 8.5$ GPa, $E = \dot{\epsilon}_{II}^{VP}$, $H = 525$ kJ/mol, and $\dot{\epsilon}_0 = 5.7 \times 10^{11}$ s^{-1} (Evans & Goetze, 1979). For the mantle lithosphere, we use at every location the smallest viscosity out of the effective viscosities for dislocation and Peierls creep.

The strength of all material phases is limited by a yield function, τ_y, defined by the Drucker-Prager criterion:

$$\tau_y = b\cos(\phi) + P\sin(\phi) \tag{12}$$

where b is cohesion and ϕ is angle of internal friction. In case of yielding, the effective viscosity is iteratively reduced until the corresponding stress invariant equals the yield stress (e.g., Lemiale et al., 2008). Therefore, the effective viscosity accounts for both plastic and viscous behavior (viscoplastic formulation) and follows the condition:

$$\eta = \eta \qquad if \quad \tau_{II} - \tau_y < 0 \tag{13}$$

$$\eta = \frac{\tau_y}{2\dot{\epsilon}_{II}} \qquad if \quad \tau_{II} - \tau_y \geq 0 \tag{14}$$

where $\dot{\epsilon}_{II}$ is the square root of the second invariant of the strain rate tensor and takes the form of

$$\dot{\epsilon}_{II} = \sqrt{\dot{\epsilon}_{11}^2 + \dot{\epsilon}_{12}^2} \tag{15}$$

The equation of energy conservation includes contributions from heat transfer, radiogenic heat production H_R, and viscoplastic dissipation H_D:

$$\rho c\frac{\partial T}{\partial t} = \frac{\partial}{\partial x_i}\left(k\frac{\partial T}{\partial x_i}\right) + H_R + H_D \tag{16}$$

where c is specific heat, k is thermal conductivity and H_D is given by

$$H_D = \frac{\tau_{11}^2}{2\eta} + \frac{\tau_{22}^2}{2\eta} + \frac{\tau_{12}^2}{\eta}\,. \tag{17}$$

The model is consistent with respect to energy conservation and involves a complete conversion of mechanical work into heat and elastic energy. We do not consider microstructural work (e.g., grain size evolution) or metamorphic reactions. The energy conservation equation is treated in a Lagrangian manner, therefore, no advection term is included in the heat transfer equation.

The above thermo-mechanical equations are solved using the finite element method. The numerical algorithm uses the MILAMIN flow solver (Dabrowski et al., 2008) and uses seven-nodes isoparametric triangular elements with quadratic shape functions for the temperature/velocities and discontinuous linear shape functions for the pressure. The computational mesh is generated with the Triangle library (Shewchuk, 2002). The mesh is deformed at each time step and remeshing is applied if the minimum angle of a triangle is less than 30.5°. In our models, the average numerical resolution is typically ~330'000 numerical finite element nodes

and the distance between the corners of the finite element triangles is typically ~600 m. For each time step, typically five Picard iterations are performed due to the nonlinear flow law and plasticity. The convergence criterion (or iteration exit criterion) is based on differences in velocities between consecutive iteration steps. Iterations are stopped when the maximum (for all nodal points) relative velocity difference (i.e., velocity difference between current and previous iteration step, divided by current velocity) between two iterations is smaller than 10^{-3}. A more detailed description of the algorithm and numerical tests is provided in Schmalholz et al. (2014).

2.2. Model Configuration

In their analytical study, Fletcher and Hallet (1983) considered a plastic layer, which represents the upper, brittle part of the lithosphere, resting on a weaker viscous layer, which represents the lower, ductile part of the lithosphere (deformation by dislocation creep). The base of the plastic layer (mimicking the brittle-ductile transition in the lithosphere) is not straight but exhibits a small-amplitude sinusoidal perturbation. As a result, when the model is extended, deformation focuses where the plastic layer is the thinnest.

In thermo-mechanical models, the crust and mantle are usually defined by distinct compositions. The deformation behavior (brittle-plastic or viscous) of the crust and mantle varies with depth and time due to the dependence of deformation behavior on temperature, pressure, and strain rate; thus, we cannot impose a sinusoidal perturbation on the brittle-ductile transition. We perturb the crust-mantle boundary sinusoidally instead, in order to generate a thicker crust in the center of the model (Figure 2). The thicker crust causes a slightly warmer model center due to increased radioactive heating, hence slightly weaker due to the reduced viscosity. The amplitude of the thickness variation is 2.5 km and distributed over the entire model width, so that the model width corresponds to the wavelength of the sinusoidal thickness variation.

To investigate the effect of the nature of extensional boundary conditions and the influence of the rheological architecture of the lithosphere, we consider three different model settings (Models 1, 2, and 3; Figure 2). These models are 300 km wide and 125 km deep. The numerical model domain extends horizontally and thins vertically during the deformation due to mass (volume) conservation. Free slip is applied on the two lateral and bottom boundaries and the top boundary is a free surface. The temperature at the base of the model is 1380 and 0°C at the surface. Radiogenic heat production has a constant value of 0.5 $\mu W/m^3$ within the entire crust and is zero in the mantle. For the sake of simplicity and faster model calculation, our models do not include an asthenosphere. This approximation is reasonable because we focus on the early stages of lithospheric extension, when the crust is relatively thick (between ~30 and 10 km thick).

With Models 1 and 2, we test the impact of the nature of boundary conditions, namely, constant bulk strain rate extension versus constant velocity extension. Both models have a similar lithospheric architecture (Figure 2a), where the crust is entirely comprised of feldspar and the mantle of dry olivine (see Table 1 for detailed physical properties). The lower crust is weak and ductile thus acts as a decoupling layer between the brittle upper crust and upper mantle. We chose feldspar rather than wet quartz to model continental crust because, for the sake of simplicity, we aimed to use one single phase to model continental crust; yet using wet quartz leads to an extremely ductile crust, which tends to thin by pure shear rather than to neck.

Model 1 is extended at a constant strain rate of $10^{-15}s^{-1}$, while Model 2 is extended at a constant velocity of 1 cm/year. In both cases, velocity boundary conditions are applied orthogonal to the model boundaries, but in Model 1 the velocity is divided by the distance between the model boundaries at each time step to generate a constant bulk rate of deformation. Models 1 and 2 have initially comparable extension rate and velocity, since when converting the bulk extension rate into an extension velocity at the model side, and conversely, using the formula $\dot{\epsilon} = v/L$ (where $\dot{\epsilon}$ is the strain rate, v the velocity, and L the width of the model) we obtain $10^{-15}s^{-1} \rightarrow 0.9$ and 1 cm/year $\rightarrow 10^{-15}s^{-1}$, respectively (only valid for $L = 300$ km). We also used a variation of Model 1, for which we turned off the density dependence on temperature and pressure to quantify the effect of thermal support.

With Models 1 and 3, we test the impact of the strength distribution within the lithosphere. In contrast to Model 1, Model 3 comprises a 15-km-thick mafic granulite lower crust, which renders the upper part of the lithosphere entirely brittle and the crust coupled to the upper mantle (Figure 2b). Both models are extended at a constant strain rate of $10^{-15}s^{-1}$.

Table 1
Feldspar (Anorthite 60) Flow Law After Rybacki and Dresen (2004); Olivine (Dry) Flow Law After Hirth and Kohlstedt (2003); Mafic Granulite Flow Law After Wilks and Carter (1990)

	Q (kJ/mol)	n	A ($Pa^{-n} \cdot s^{-1}$)	ρ (kg/m^3)	k ($W \cdot m^{-1} \cdot K^{-1}$)	H ($\mu W/m^3$)	ϕ (°)	b (MPa)	α ($°C^{-1}$)
Feldspar	253	3	$3.16e^{-20}$	2,690	2.5	0.5	30	10	$3.20e^{-5}$
Mafic granulite	445	2	$1.40e^{-8}$	2,900	2.1	0.5	30	10	$3.20e^{-5}$
Dry olivine	520	3.5	$1.6e^{-18}$	3,300	3	0.5	30	10	$3.20e^{-5}$

Note. Physical parameters used in the models. Q = activation energy; n = stress exponent; A = pre-exponential term; ρ = density at reference temperature 0 K; k = thermal conductivity; H = radiogenic heat production; ϕ = internal angle of friction; b = cohesion; α = coefficient of thermal expansion.

Finally, to investigate the impact of the initial Moho perturbation wavelength, we designed three series of models, namely, Model Series 1, 2, and 3. The initial rheological architecture (phases distribution and geotherm) as well as the extensional boundary conditions are identical to those of the corresponding Models 1, 2, and 3, but we test various initial Moho perturbation wavelengths, namely, 150, 180, 200, 220, 240, 260, 300, 350, 400, 600, 800, and 1,200 km. In these series, the initial width of the model corresponds to the perturbation wavelength (Figures 2a and 2b), as in the analysis by Fletcher and Hallet (1983).

3. Results

3.1. Individual Models

3.1.1. Model 1: Decoupled Crust/Mantle and Constant Bulk Extension Rate

Figure 3a shows that Model 1 topography is slightly higher in the center during the early stages of model evolution as a consequence to the locally thickened crust. As extension continues the model center deepens progressively to about 3.5 km, while a ~2-km-high topography develops on either side (the so-called rift shoulders). Figure 3a highlights that the width of the central subsiding region remains largely constant throughout the models evolution. The evolution of Moho topography is relatively complex and not identical to the surface topography evolution. Indeed, between 0 and ~5 Myrs the Moho remains relatively deep in the center of the model, while it is shallower on either side and deepens again towards the model's edges (Figure 3d).

The evolution of the crust and mantle thinning at the rift center (Figure 3g) shows that crustal and mantle necking are not identical ("mantle thinning" corresponds to the vertical distance variation between the Moho and the base of the model at a given time compared to the initial stage). Three main stages can be identified: Between 0 and 1.8 Myrs of extension, both the crust and the mantle are progressively attenuated by ~4 km. Between 1.8 and 4 Myrs crustal thinning slows down drastically and the crust even thickens subsequently by approximately 1.3 km. In contrast, in the same time interval, the mantle thins progressively to reach ~13 km. Finally, from 4 Myrs onward, the crust is intensively thinned by ~19 km (from ~29 to 10 km) in less than 4 Myrs, while mantle thinning slows down drastically and mantle thickens subsequently by ~6 km at the rift center.

Five phases can be distinguished when looking at the surface topography evolution (Figure 3j): From 0 to 0.7 Myr the topography increases from 0 to 0.7 km, which reflects the isostatic equilibration of the initially flat surface of the model above the thickened crust. As the stresses are still building up viscoelastically during this stage, significant necking has not started yet, neither in the crust, nor in the mantle. Therefore, we argue that the initial isostatic re-equilibration has no significant impact on the necking processes per se. Between 0.7 and 2.7 Myrs the topography decreases from 0.7 to −1.7 km. Between 2.7 and 4.8 Myrs, the center of the rift remains stable at −1.7 km. This stable topography is also observed in the model with constant density (see the solid green curve on Figure 3j), which suggests that the lack of subsidence is not due to a thermal support. The fact that the plateau is deeper in the constant density model (−2.7 km instead of −1.7 km in Model 1) is a result of the globally increased density induced by the absence of thermal expansion. Between 4.8 and 6.6 Myrs the topography decreases from −1.7 to −3.6 km and remains at −3.6 km until the crust is thinned to 10 km, that is, slightly before 8 Myrs. The last phase without surface subsidence is not observed in the model with constant density (solid green curve on Figure 3j), which suggests that it is a consequence of the thermal support from the underlying upwelling mantle.

There is no obvious correlation between the altitude evolution of the surface topography and the crustal or mantle thinning evolution at rift center (compare Figures 3g and 3j). The onset of the first phase of surface topography stability (at 2.7 Myrs) is coeval with the onset of crustal thickening and the end of this phase of

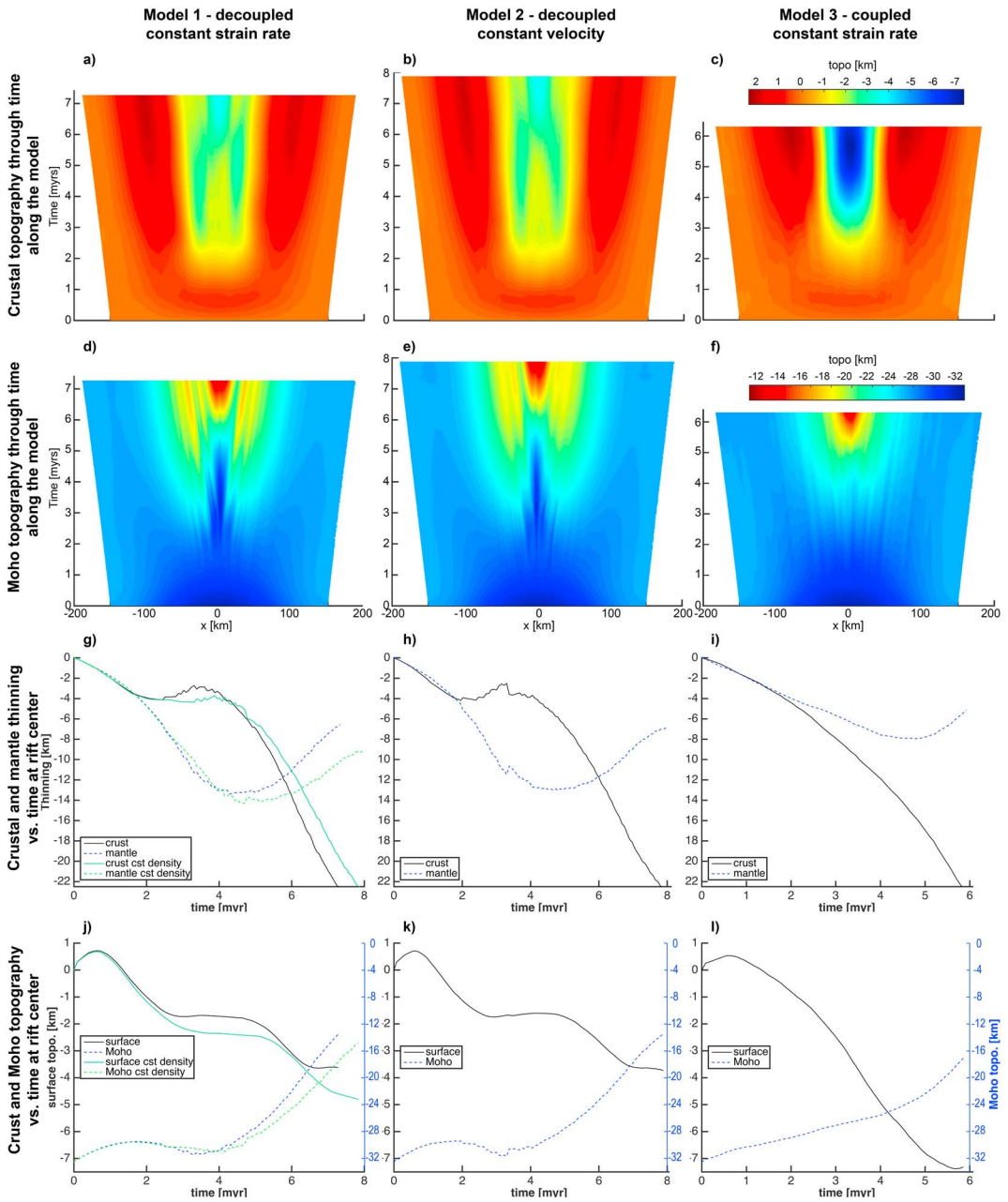

Figure 3. (a–c) Surface topography through time along the models; (d–f) Moho topography through time along the models; (g–i) Changes in crustal (solid line) and mantle (dashed line) thickness versus time at the center of the rift for Model 1 (black and blue) and Model 1 with constant density (green), Model 2 and Model 3. "Mantle thinning" corresponds to the vertical distance variation between the Moho and the base of the model at a given time compared to the initial stage; (j–l) Surface (solid line—left-hand axis) and Moho (dashed line—right-hand axis) topography versus time at the center of the rift for Model 1 (black and blue) and Model 1 with constant density (green), Model 2 and Model 3. The initial thickness H_0 at the center of the rift is 32.5 km. The end of necking is defined as the time when crustal thickness is reduced to 10 km.

surface topography stability (at ~4.8 Myrs) corresponds to the onset of mantle thickening. However, the three crustal thinning phases identified in Figure 3g can be related to the evolution of the Moho topography in Figure 3j, whose absolute depth variations (~20 km) are almost five times higher than those of the surface topography (~4 km).

Figures 4a to 7a display the main thermo-mechanical characteristics for each of the three stages of thinning described above. The first panel of Figure 5a shows that during the early stages of extension (from

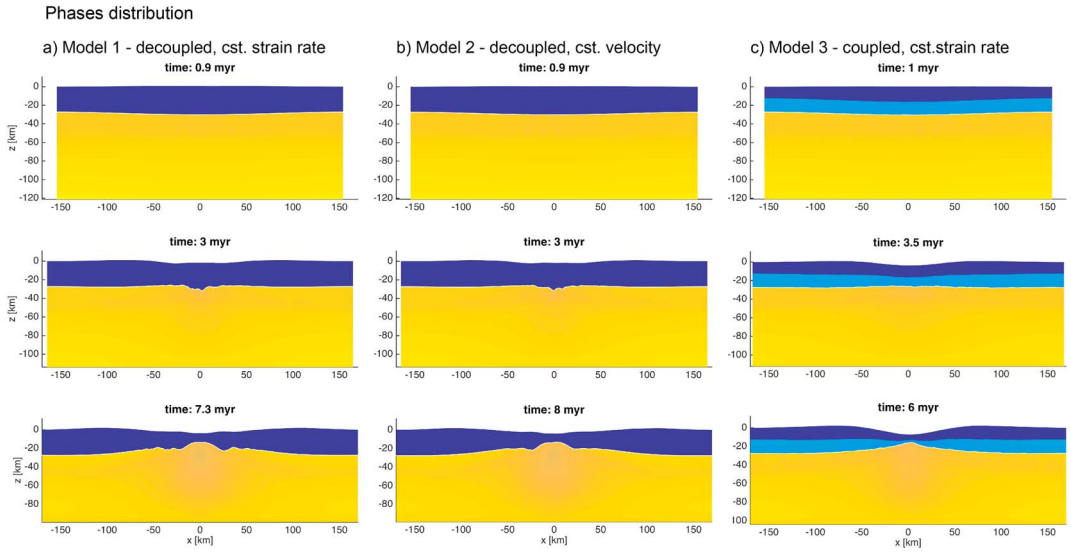

Figure 4. Distribution of crustal and mantle material at different stages of extension: (a) Model 1, (b) Model 2, and (c) Model 3. Dark blue: feldspar; light blue: mafic granulite; yellow: olivine.

0 to ~1.5 Myrs) deformation is widely distributed in both the crust and the upper mantle. Neither the deviatoric horizontal stress distribution nor the geothermal gradient is significantly modified at this stage (Figures 6a and 7a).

Upon further extension, from ~1.7 to 4 Myrs, crustal deformation becomes more localized within two wide conjugate shear zones on either side of an undeformed block (the so-called keystone, Pèron-Pinvidic & Manatschal, 2010, or H-block, Lavier & Manatschal, 2006; see middle panel of Figure 5a). Beneath this block, the Moho is deeper than anywhere else in the model (Figure 4a). Both crustal shear zones root in a thin high strain rate zone at the base of the crust (middle panel of Figure 5a), which is interpreted as a décollement surface. In the mantle, deformation is localized in two relatively narrow and intensively deforming shear zones. The middle panel of Figure 6a highlights that the strong part of the mantle (initially between 30 and 60 km depth; see depth-dependent stress profile in Figure 2a) is significantly attenuated at the rift center, in contrast

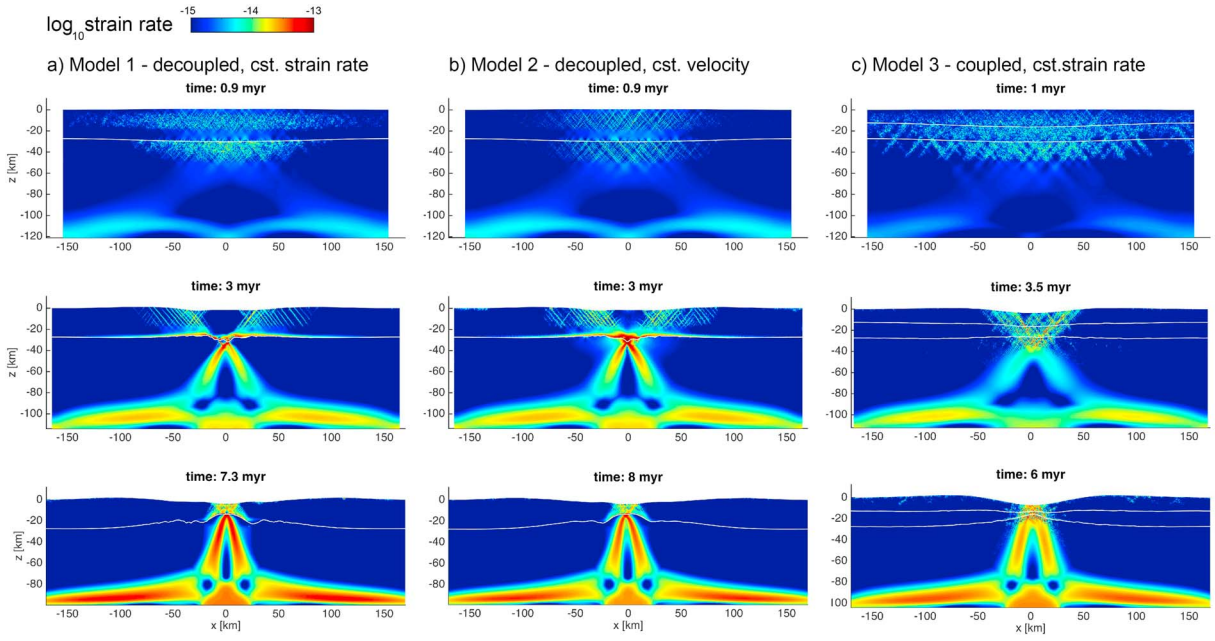

Figure 5. Second invariant of the train rate tensor (equation (15) across the models at different stages of extension: (a) Model 1, (b) Model 2, and (c) Model 3.

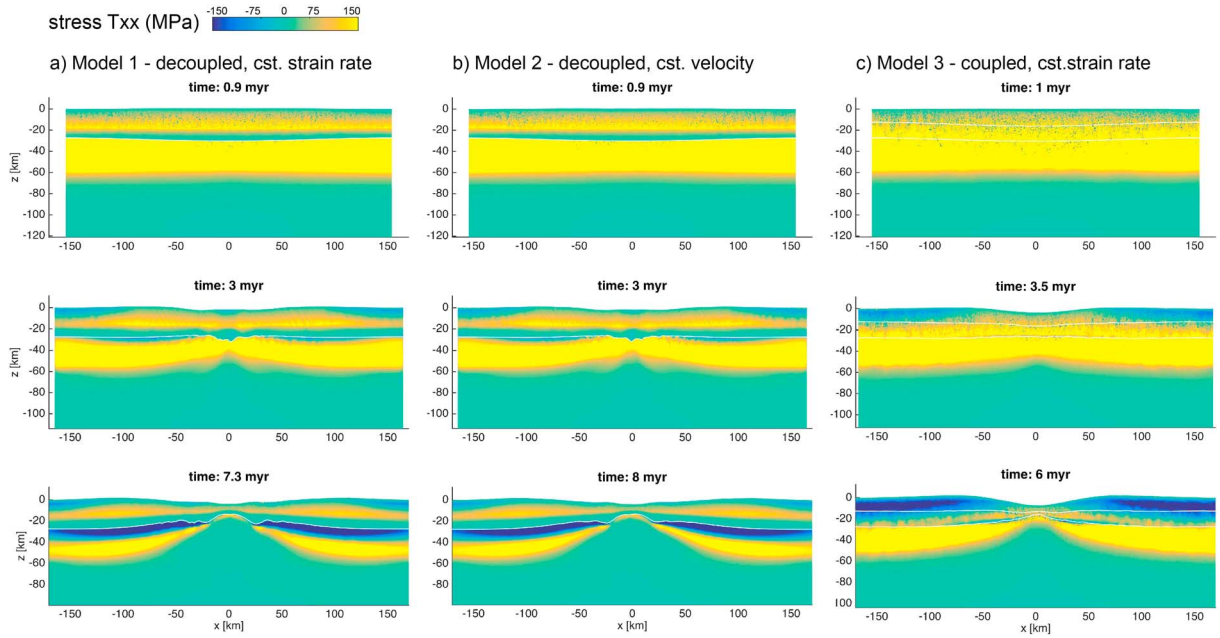

Figure 6. Horizontal deviatoric stress across the models at different stages of extension: (a) Model 1, (b) Model 2, and (c) Model 3. Negative values reflect compression and positive values extension.

to the crust. The middle panel of Figure 7a shows that temperature increase is already significant in the center of the rift (the Moho temperature at the rift center is close to 800°C), although asthenospheric convection is not modeled.

From ~6 Myrs to the end of crustal necking, deformation is localized in a narrow region in both the crust and the mantle (Figure 5a). At this stage, the 1300°C isotherm is only 45 km deep, which may account for the retardation in subsidence observed at the end of the simulation (Figure 3k). Both the crust and the uppermost mantle have lost most of their strength in the central part of the model as shown by the significant decrease in the absolute values of horizontal deviatoric stress in this region (Figure 6a). On both sides of the central

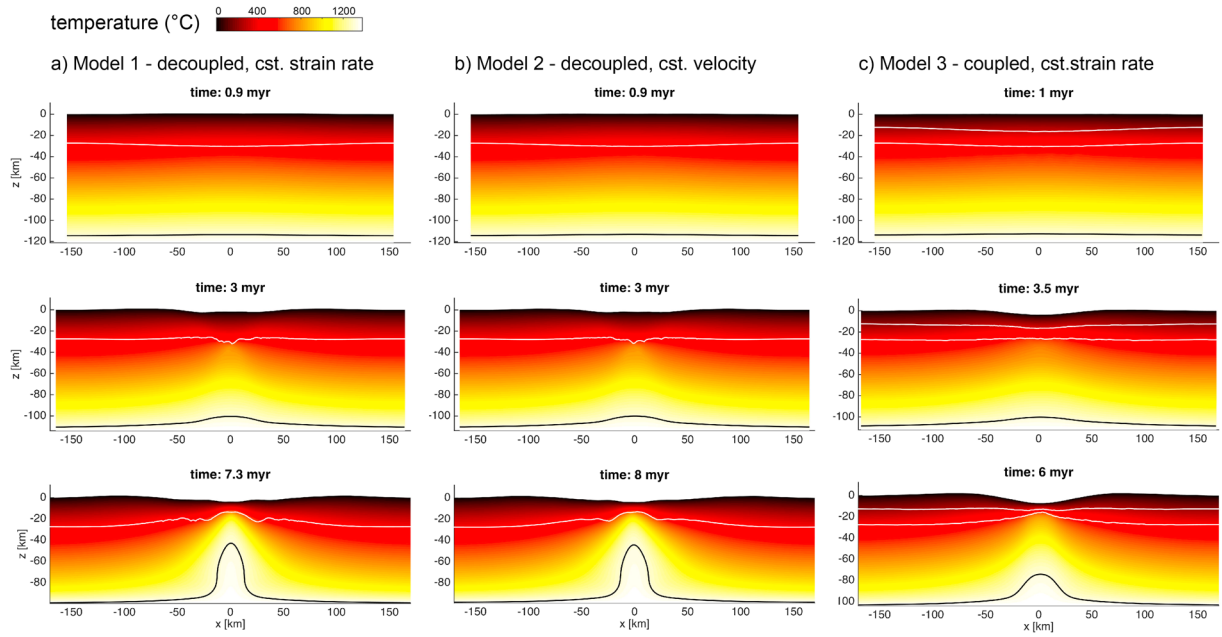

Figure 7. Temperature across the models at different stages of extension: (a) Model 1, (b) Model 2, and (c) Model 3. The black line represents the 1300°C isotherm.

region the uppermost (strong) part of the unattenuated mantle undergoes compression, while the lower part undergoes extension. This state of stress reflects the bending of the upper mantle towards the surface in the model center, which is mainly caused by the isostatic equilibration of the overdeepened Moho. Indeed, as the level of necking (around the lower crust/upper mantle brittle-ductile transition) is above the level of isostatically compensated depth (here the base of the model), buoyancy forces tend to bring the Moho upward toward its local isostatic balance (Braun & Beaumont, 1989; Weissel & Karner, 1989). Additional processes affecting the bending can be the thermal support of the upwelling underlying mantle and/or the elastic response to the thinning of the overlying crust.

The formerly overthickened crustal central region is split in two regions by the upwelling of the mantle, which forms regions of relatively thick continental crust on either side of the thinnest (central) region (see the bottom panel of Figure 4a). In the following sections, we refer to these regions of thick crust as "continental lumps."

3.1.2. Model 2: Decoupled Crust/Mantle and Constant Velocity Extension

The results of Model 2 are similar to the ones of Model 1 (compare panels (a), (d), (g), and (j) to (b), (e), (h), and (k) in Figure 3). The evolution of surface and Moho topography, crustal and mantle thinning versus time as well as the evolution of surface and Moho topography at the rift center are comparable. The same stages can be recognized in both plots, with similar timing and amplitudes. The evolution of the thermo-mechanical quantities is also similar between Models 1 and 2 (compare panels (a) and (b) in Figures 4 to 7) and continental lumps do form on either side of the thinnest region as well (Figure 4b, bottom panel).

3.1.3. Model 3: Coupled Crust/Mantle and Constant Bulk Extension Rate

The results of Model 3 contrast widely with the ones of Model 1 (compare panels (a) and (c) in Figures 3 to 7). The subsiding region is slightly narrower than in Models 1 and 2 (compare Figures 3c to 3a), and it reaches a deeper level (up to 7 km below sea level). The Moho topography evolution is monotonic unlike those in Models 1 and 2, since the Moho is shallower beneath the model center during the entire model evolution (Figure 3f).

In Model 3, the crust thins gently but constantly throughout the simulation (Figure 3i). Mantle thinning is approximately constant between 0 and 4 Myrs, before the thinning slows down and the mantle starts thickening until the end of the simulation at 5.8 Myrs. The topography at rift center decreases progressively as extension progresses (Figure 3l), except during the initial isostatic equilibration and at the very end of the necking, where topography increases and remains stable, respectively. For the latter stage, thermal support of the upwelling mantle is a likely candidate to explain the decrease and lack of subsidence (see bottom panel of Figure 7c).

Figure 5c shows that extension is initially accommodated by distributed deformation within both the crust and the mantle. This stage is slightly longer compared to that of Model 1 (2.5 versus 1.5 Myrs, respectively). As extension progresses, deformation concentrates progressively towards the model center affecting an ever narrower region at ever higher strain rate, without forming a keystone block. Extension is accommodated by a series of conjugate shear zones, which crosscut the entire crust and uppermost mantle (Figure 5c). Here the entire brittle layer (crust and upper mantle) is bending upward, which translates into compression within the crust as opposed to extension within the mantle (Figure 6c). In Model 3, no continental lump is formed at any stage of extension (Figure 4c).

3.2. Model Series

3.2.1. Model Series 1: Decoupled Crust/Mantle and Constant Bulk Extension Rate

Figure 8a shows that the duration of necking decreases exponentially with increasing initial perturbation wavelength. In the narrowest model (150 km), necking is completed after 13.6 Myrs extension, after 8.8 Myrs in the 200-km wide model and after only 4.1 Myrs in the 1,200-km wide model.

The evolution of crustal thinning versus normalized time is similar for all the models of the series (Figure 8d), comprising two phases of relatively intense crustal thinning separated by one phase of reduced thinning (hence thickening in some models). In contrast mantle thinning is more variable, which impacts the amplitude of the surface topography vertical movements (Figures 8g and 8j). The general trend is as follows: The larger the perturbation wavelength, the smaller the mantle thinning and the higher the surface topography at rift center. For the narrower models (between 150 and 400 km wide), the narrower the models/perturbations, the further away from the theoretical pure shear isostatic equilibrium (red dashed line on Figure 8j) the models. The 300-, 400-, and 800-km wide models are the closest to the isostatic equilibrium. This can be explained by

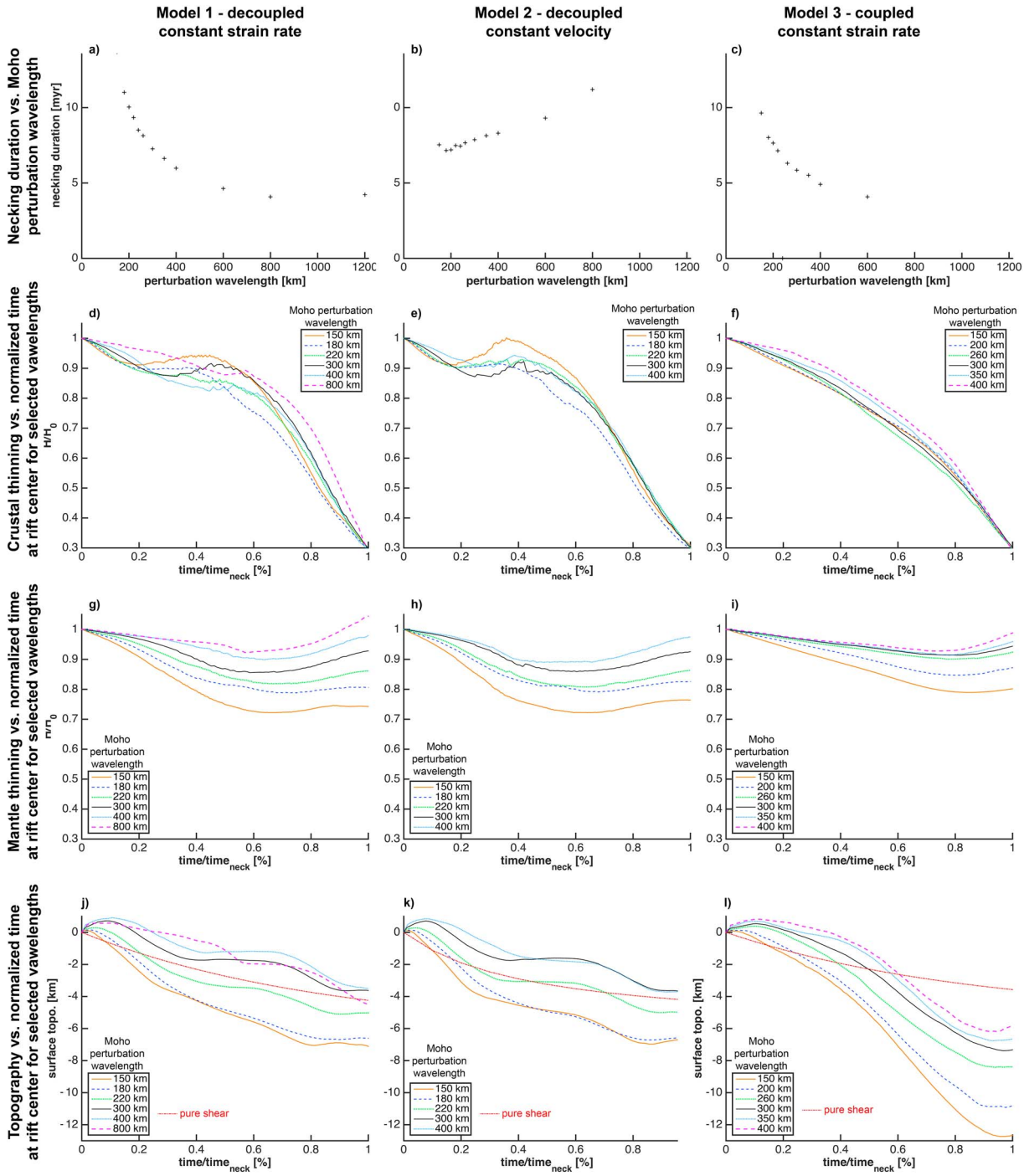

Figure 8. (a–c) Duration of necking versus initial Moho perturbation wavelength; (d–e) crustal thinning (%) at the rift center versus normalized time (i.e., time/total necking duration); (f–i) Mantle thinning (%) at the rift center versus normalized time; and (j–l) Topography evolution versus crustal thinning for Model Series 1, 2, and 3. The red dashed lines labeled "pure shear" in panels (j)–(l) represent the theoretical topography versus normalized time evolution for an equivalent model thinned by pure shear at a same strain rate ($10^{-15}s^{-1}$).

the higher flexural allowance of wider models due to the increased distance between the model edges, where the boundary conditions are imposed.

Figure 9a highlights that, in the earliest stage of extension, strain rate has a comparable magnitude in the narrow (200 km—left-hand panel) and the wide (800 km—right-hand panel) models. With progressive necking however, strain rates become significantly larger in the wide model than in the narrow one.

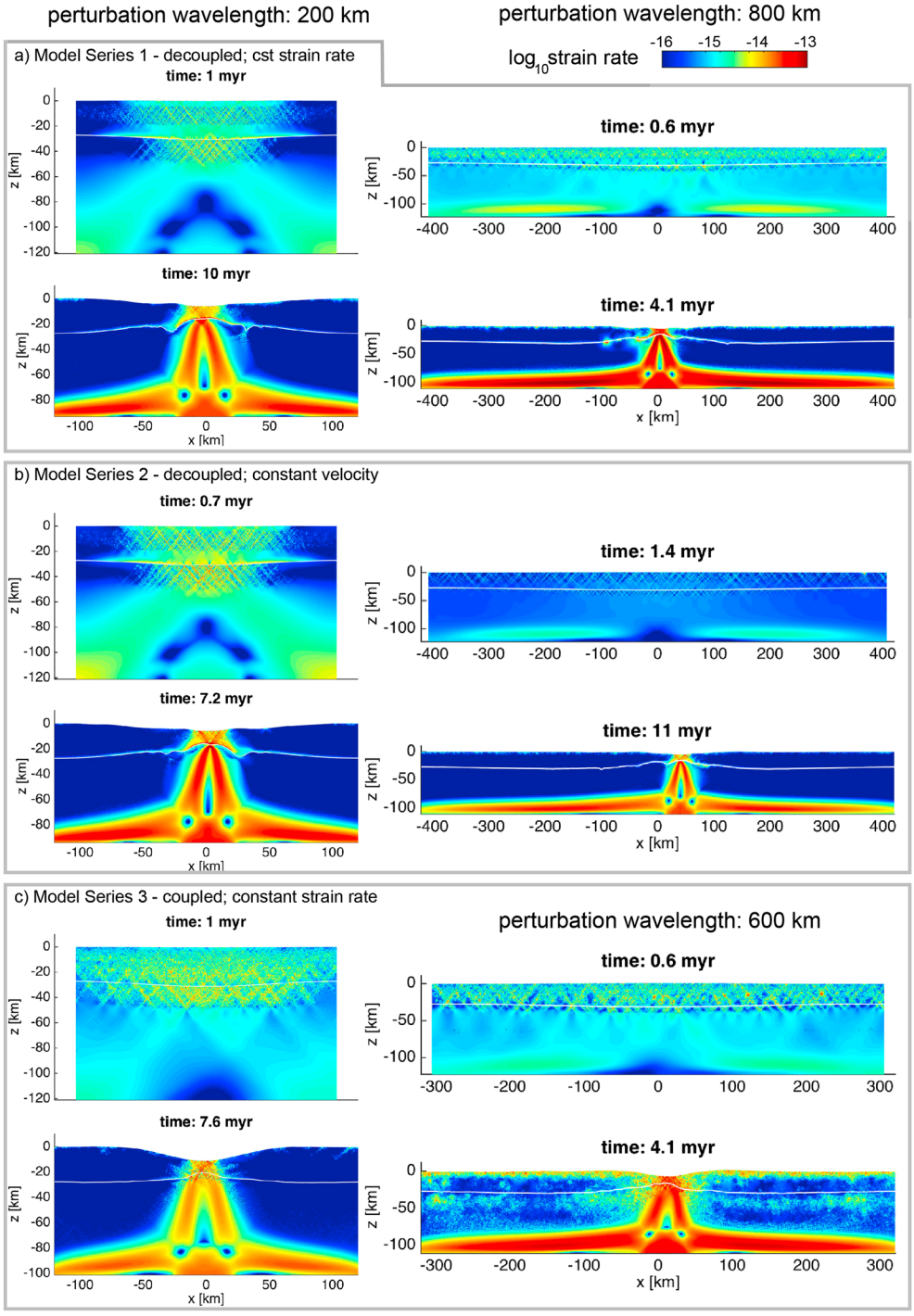

Figure 9. Log_{10}(second invariant of the strain rate tensor) in the 200 km (left) and 800 km (right) wide models of Model Series 1 (a), 2 (b), and 3 (c).

For each model, we measured the width of the conjugate necking zones at the final stage (Figure 10 and Table 2), based on the morphological definition of necking zones defined by Sutra et al. (2013) and highlighted on Figure 1. For our models, we defined the necking zone width as the distance between the onset of top basement deepening/Moho shallowing and the center of the rift at the end of the simulation (approximately end of the necking stage). For several model results, the inflection in top basement is significantly laterally offset from that in the Moho (Figure 10). In such cases, we placed the necking point at the onset of crustal inflection, consistent with Chenin et al. (2017) for their necking zones width measurements when the Moho

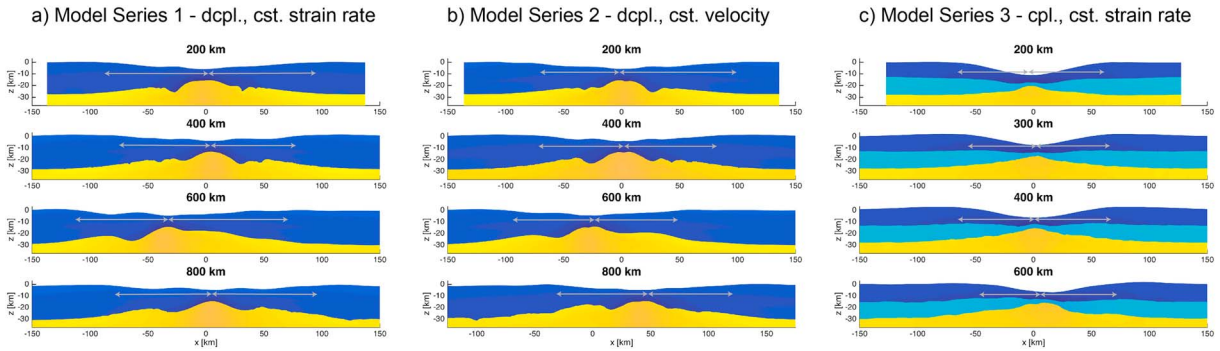

Figure 10. Zoom on the crustal necking zone of models with a different initial Moho perturbation wavelength for (a) Model Series 1, (b) Model Series 2, and (c) Model Series 3. The arrows represent the extent of the conjugate necking zones.

was not well resolved on the seismic sections they used. In the models of Series 1, the width of the necking zones at the end of the simulation range consistently between 65 and 105 km with an average of 80 km (Figure 10a and Table 2).

In most models, one continental lump can be identified on each side of the central region of most intense necking. The 600-km wide model on Figure 10a is an illustrative counterexample, with only one, but larger, continental lump on the left-hand side of the rift center. In this model, the final necking zone is offset by ~30 km to the left from the model center. The reason for this architecture is that necking of the upper mantle started slightly to the left of the central region, whereas crustal necking localized closer to the center. As a result, instead of splitting the keystone block in two, necking localized on its right-hand side, leaving it almost intact. Theoretically, in such a model with a symmetrical physical properties distribution, necking of the crust should be symmetric. However, due to the very weak initial perturbation and the related diffuse character of the deformation, any small numerical perturbation (e.g., numerical round-off errors or truncation of numerical

Table 2
Table Summarizing the Width of the Left-Hand (L) and Right-Hand (R) Necking Zone for the Models of Series 1, 2, and 3

	Model Series 1		Model Series 2		Model Series 3	
Pert. wvl (km)	L	R	L	R	L	R
150	—	—	—	—	65	70
180	105	100	90	75	65	70
200	70	100	90	95	60	65
220	95	90	70	70	60	65
240	70	75	65	75	55	55
260	70	65	75	70	60	60
300	80	80	65	70	55	60
350	75	70	70	80	60	60
400	75	80	80	75	65	65
600	70	70	80	105	50	65
800	80	75	85	90	—	—
1200	85	80	105	45	—	—
minimum	65		45		50	
average	80		78		62	
maximum	105		105		70	

Note. The width of the necking zone corresponds to the distance between the onset of top basement deepening and the center of the rift (see Figures 1 and 10). The width of the necking zones could not be measured for the 150-km wide model of Model Series 1 and 2 because they reached the edges of the models. No necking zone did form in the 800- and 1,200-km wide models of Model Series 3 because they thinned by pure shear only.

iteration schemes necessary to treat the rheological nonlinearities) on the unstructured, hence asymmetric, numerical mesh can cause a slight shift of the necking centre, and thus asymmetrical evolution of the model. Such unavoidable numerical perturbations could be considered as effect of small and randomly distributed natural heterogeneities in material properties.

3.2.2. Model Series 2: Decoupled Crust/Mantle and Constant Velocity Extension

The relationship between necking duration and perturbation wavelength is completely different in Model Series 2 and 1. Instead of the systematic decrease in the necking duration with increasing perturbation wavelength observed in Model Series 1, we observe a generally increasing duration with increasing wavelength in Model Series 2 (Figure 8b). We notice a minimum in necking duration for the perturbation wavelength of 180 km. Nevertheless, crustal thinning, mantle thinning and surface topography evolution are comparable in both Series (compare Figures 8d, 8g, and 8j to 8e, 8h, and 8k).

Figure 9b shows that, during the earliest stage of extension, strain rate is significantly lower in wide models than in narrow ones. Later however, strain rate becomes similar in the narrow and wide models. This behavior contrasts significantly with the one observed for Model Series 1 (Figure 9a). Nevertheless, necking zones widths in Model Series 2 are close to those of Model Series 1, ranging from 45 to 105 km with an average of 78 km (see Table 2 and compare panels (a) and (b) in Figure 10).

3.2.3. Model Series 3: Coupled Crust/Mantle and Constant Bulk Extension Rate

The relationship between necking duration and perturbation wavelength is similar in Model Series 3 and 1, showing an exponential decrease of the duration with increasing perturbation wavelength (Figure 8c). For a similar perturbation wavelength however, the duration of necking is consistently shorter in Model Series 3 compared to Model Series 1. For the largest perturbation wavelengths (800 and 1,200 km) of Model Series 3, the models predict no necking but only distributed thinning over the entire model domain.

The models of Series 3 show a remarkable consistency in the evolution of crustal thinning versus normalized time (Figure 8f). The evolution of mantle thinning is also relatively similar among the different models of Series 3 (Figure 8i), in contrast to Model Series 1 and 2. However, there is a significant difference in the evolution of surface topography at rift center among the models of Series 3, much larger than in the two other series. For Model Series 3, the depth of the rift center at the end of necking is −13 km in the 150-km wide model, while it is −6 km in the 400-km wide model. These values are far below the prediction of the pure shear theory in all models (red dashed line in Figure 8l).

Figure 9c indicates that strain rate is comparable in the early stage of extension between narrow and wide models, but strain rate becomes much higher in the wide model than in the narrow one in later stages. This behavior is comparable to that observed in Model Series 1 (Figure 9a). The width of the necking zones in Model Series 3 ranges between 50 and 70 km, with an average of 62 km (Figure 10c and Table 2). Theses values are of the same order than those of Model Series 1 and 2 (45–105 km), although generally slightly smaller.

4. Discussion

4.1. The Impact of Crust-Mantle Coupling

4.1.1. General Evolution

In all models where the crust is mechanically decoupled from the mantle by a ductile lower crust (Model Series 1 and 2), three phases in the evolution of crustal thinning versus time can be identified (Figure 11a): (1) a phase of moderate crustal thinning where deformation is widely distributed within the crust and mantle (stretching phase); (2) a phase of extreme slowing in crustal thinning with sometimes a relative crustal thickening, which reflects the necking of the upper mantle and associated flow in the lower crust towards the necking area; and (3) a phase of intense crustal thinning associated with the necking of the crust following the loss of the upper mantle strength and its flexural rebound. These three phases correspond to these described by Lavier and Manatschal (2006), whose models included a strain softening mechanism. While the duration of the first phase (stretching) and second phase (upper mantle necking) are relatively variable amongst models, the third phase (crustal necking) generally starts after ~45% of the total duration of necking (Figures 8d and 8e). In contrast, when the crust and upper mantle are mechanically coupled and fully brittle-plastic (Model Series 3), only two phases can be identified (Figure 11b), namely, (1) a phase of moderate crustal thinning where deformation is widely distributed within the crust and mantle (stretching phase) and (2) a phase of intense crustal and upper mantle necking leading to a rapid thinning of the crust to 10 km.

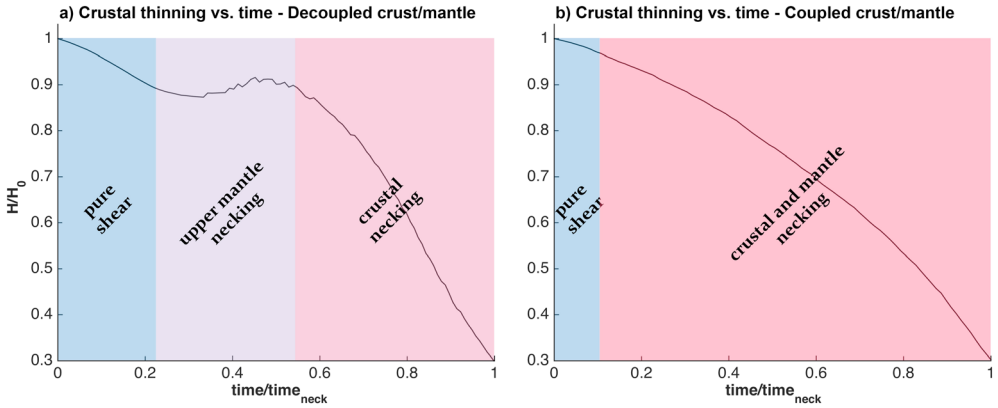

Figure 11. Crustal thinning versus normalized time at the rift center for models with (a) decoupled crust and mantle and (b) coupled crust and mantle.

The existence of the early stretching stage in both models is related to the small amplitude and large width of the crustal thickness perturbation. Indeed, all numerical models of lithospheric rifting that do not rely on a week seed or a localized thermal anomaly to force the localization of deformation start with a stage of distributed deformation (Huismans & Beaumont, 2007; Jammes & Lavier, 2016; Lavier & Manatschal, 2006), in contrast to the others (see Dyksterhuis et al., 2007, for a review). Generally, for a sinusoidal initial perturbation of given wavelength, the initial amplitude of the perturbation has a strong impact on the duration of the initial distributed thinning phase: The smaller the initial amplitude the longer the initial phase of distributed thinning. In models with a smooth and wide perturbation, whether localized deformation first occurs in the crust or in the upper mantle depends (i) on the location of the perturbation (i.e., within the crust, the mantle, both the crust and the mantle or at the crust-mantle boundary); (ii) on the coupling intensity between the crust and the mantle; and (iii) on the rheology contrast between the layer containing the perturbation and the other layers (Chenin & Beaumont, 2013; Dyksterhuis et al., 2007; Jammes & Lavier, 2016). In our models, the perturbation affects both the crust and the mantle. In our decoupled models (Model Series 1 and 2), the mantle is significantly stronger (exhibiting higher differential stresses) than the crust; therefore, it necks first and controls subsequent thinning. In contrast, there is no abrupt change in strength/stiffness across the Moho in our coupled models (Model Series 3); therefore, the entire brittle-plastic part of the lithosphere is necked as one effective single layer.

4.1.2. General Rift Architecture

Neither the nature of extensional boundary condition (constant strain rate versus constant velocity extension) nor the wavelength of the initial Moho perturbation (from 150 to 1,200 km), nor the existence of a decoupling layer between the crust and mantle have a major effect on the width of the modeled necking zones (Figure 10 and Table 2). The width of necking zones ranges between 65 and 105 km in Model Series 1 (decoupled models) and between 50 and 70 km in Model Series 3 (coupled models). These ranges are consistent with both the predictions from analytical studies (14–83 km according to Schmalholz & Mancktelow, 2016; see also Appendix A2) and the width observed at natural rift systems/margins (10–100 km according to Chenin et al., 2017; see Figure 1b). The generally narrower width of necking zones in the coupled models with respect to decoupled models is consistent with the results of previous studies, which predict wider rift zones for weaker lithospheres (for instance, Bassi, 1991; Buck, 1991).

In models where the crust is decoupled from the mantle by a ductile lower crust (Model Series 1 and 2), the later necking of the crust compared to that of the upper mantle may explain the existence of regions of locally thick/unthinned continental crust (continental lumps) at rifted margins (e.g., Galicia, Rockall, Hatton, and Porcupine Banks in the North Atlantic; Pèron-Pinvidic & Manatschal, 2010). In Models 1 and 2, comparable continental lumps form because the region of crustal necking is narrower than that of upper mantle necking (Figures 4a and 4b). This phenomena does not exist when the crust is coupled to the mantle (Figure 4c); therefore, we suggest that the existence of continental lumps may sometimes only reflect the existence of ductile levels in the initial continental crust, without the need of preexisting lateral strength heterogeneities (Vink et al., 1984), mantle plumes (Müller et al., 2001), or polyphase rifting (Gernigon et al., 2012; Manatschal et al., 2007; Pèron-Pinvidic & Manatschal, 2010). When the necking of the upper mantle is laterally offset form

the region of crustal necking as in the 600-km wide model of Model Series 1 (Figure 10a, third panel), the keystone block may be preserved on one side of the margin. In this example, the continental lump can be compared to the Briançonnais in the Alps, which is sometimes interpreted as a preserved "H-block" or "keystone" (Haupert et al., 2016; Lavier & Manatschal, 2006).

4.1.3. Rift Center Topography Evolution

In the decoupled models, the evolution of surface topography at the rift center is characterized by two phases of significant subsidence separated by one phase of surface topography stability (Figures 3j and 3k). This retardation of subsidence is the result of both the formation of a crustal keystone block above the area of upper mantle necking and the flow of lower crust towards this necked area. Once the upper mantle is attenuated to the degree it looses its lateral strength, the isostatic equilibration resulting from the flexural rebound and/or the upwelling of the underlying mantle bends the brittle-plastic upper mantle upward and necking of the crust starts in the wake (Figures 6 and 7).

This behavior contrasts widely with that observed for the extension of a fully brittle-plastic upper lithosphere (Model 3), where necking is a progressive process and where topography subsides continuously at the rift center (Figures 3i and 3l). These results highlight the crucial impact of the decoupling lower crust in the evolution of subsidence, and thus on the possible formation of unconformities in the sedimentary deposits of natural rift basins.

4.2. The Impact of the Nature of Extensional Boundary Conditions

Comparing the results of individual Models 1 and 2 (left-hand and central panels in Figure 3; panels (a) and (b) in Figures 4 to 7) shows that both the evolution of crustal architecture and thermo-mechanical quantities are similar when extension is controlled by a constant bulk rate or constant velocity, provided that the magnitude of extension rate and extension velocity is similar (see section 2.2). However, the duration of rifting varies significantly between Model Series 1 and 2 depending on the applied perturbation wavelength and/or model width (compare panels (a) and (b) in Figure 8). To unravel whether the effect of the perturbation wavelength or model width dominates, we ran a 300-km wide model with mechanically decoupled crust/Moho and constant strain rate (Model 1 type model) with a 150-km wavelength in the center of the model and a flat Moho on either sides (not shown here). The results showed that the duration of necking and the general model evolution are much closer to that of the 300 km than to the 150 km wavelength model of Model Series 1. Therefore, we concluded that the model width rather than the perturbation wavelength controls the duration of necking in constant strain rate models.

While necking duration decreases exponentially with increasing initial model width for constant extension rate models, we observe a globally increasing necking duration with increasing model width for constant extension velocity models, with a local minimum for the 180-km wide model. The opposite trend in necking duration versus model width between Model Series 1 and 2 can be explained by the progressive localization of deformation as extension progresses. During the initial stage of distributed deformation, strain rate intensity is comparable in the narrow and wide models of Model Series 1, which is a consequence of the constant bulk extension rate in the different models (compare top panels of Figure 9a). In contrast, strain rate is significantly lower in wide models than in narrow ones at a similar stage in Model Series 2 (compare top panels of Figure 9b) because, for a constant velocity (v), wider models (width = L) cause smaller bulk extension rates ($\dot{\epsilon} = v/L$).

The minimum rifting time for the model with an initial 180-km perturbation wavelength is consistent with the predicted dominant wavelength from the study by Fletcher and Hallet (1983). In this study, the wavelength corresponding to the largest neck amplification rate is approximately four times the thickness of the strong upper part of the lithosphere. Yet in Model Series 1 and 2, the effective thickness of the strong upper part of the lithosphere (including the intermediate ductile layer) is ~50 km thick (see depth-dependent stress profile in Figure 2a), which would be associated with a dominant wavelength of ~200 km. However, models 150 km wide or less are presumably "too narrow" for the rift zone not to be significantly affected by the lateral boundary conditions. Therefore, this minimum may not be a result of necking processes only but may be significantly influenced by boundary effects.

As extension continues, deformation localizes in a region whose width is largely independent on the initial model width and extensional boundary conditions, and this without the need of strain softening/weakening mechanisms. The necking width is likely controlled by the thickness of the brittle layer, as suggested by analytical studies on mechanical necking instabilities (e.g., Fletcher & Hallet, 1983; see middle panels of Figures 9a

and 9b), which would explain why the necking domain is of relatively constant width in all models of all series (Figure 10). The regions outside the actively deforming necking zones behave as effectively rigid units, which are displaced laterally with the constant boundary velocity. This boundary velocity applies effectively at the lateral sides of the actively necking regions, and since this region is narrower than the model width, the bulk extension rates are significantly increased. Because wider models have larger extension velocities, to maintain the same bulk extension rate the effective bulk extension rate is significantly larger in the necking domain of wide models than in the narrow ones (compare bottom panels of Figure 9a). Conversely, strain rate in the necking domain is comparable between the narrow and wide models of Model Series 2 (compare bottom panels of Figure 9b) since the same extension velocity is applied to deformation zones of comparable width.

As all models comprise a phase of distributed deformation and a phase of localized deformation, neither constant bulk extension rate boundary conditions nor constant velocity boundary conditions allow for a strict comparison between models of different width/perturbation wavelength. However, because the phase of distributed deformation is significantly shorter than that of localized deformation (Figure 11), constant velocity boundary conditions are more appropriate to compare rifting evolution between models of different width/perturbation wavelengths.

The important impact of the boundary conditions on necking duration renders the comparison between analytical studies of lithospheric necking and the presented numerical simulations of necking difficult. Indeed, many analytical solutions are strictly valid only for small-amplitude necking, that is, small lateral thickness variations, and when the deviations between the strain rate due to necking and that due to pure shear extension are assumed to be small. Yet, in the numerical simulations, the lateral thickness variations are significant due to high-amplitude necking, and the strain rate variations are consequently also significant. The analytical studies quantify the amplification rates of initial geometrical perturbations with widely varying wavelengths under the assumption that the bulk extension rate is identical for all perturbations. This requires different lateral extension velocities for the models with different wavelengths. These different extension velocities cause strain rate focusing of different magnitude once necking starts and a significant necking zone has developed. Therefore, the assumption of a constant bulk (or basic state) extension rate of the analytical studies, applicable to small amplitude necking, is not applicable for high-amplitude necking simulations.

For all simulations, the widths of necking zones range between 45 and 105 km with an average of approximately 70 km. These values correspond to total necking width between 90 and 210 km (sum of the two conjugate necking zones widths), which could be considered as extended necking wavelengths. Assuming that the effective thickness of the strong upper layer of the lithosphere in our models is approximately 50 km, the wavelength to thickness ratio in the numerical models ranges between 1.8 and 4.2, which covers the range of analytically predicted dominant wavelength to thickness ratios for lithospheric necking of approximately 3 to 4 (Fletcher & Hallet, 1983 see also Appendix A2).

The widths of the modeled necking zones are similar to those observed at natural rift systems/margins, although the modeled widths are slightly larger in average (Figure 1b). Yet our simple models do not consider a number of processes, which could intensify the necking instability such as multilayer necking effects (Duretz et al., 2016) and material softening due to grain size reduction or mineral reactions coupled to fluid flow. If such additional processes would be included in the simulations, the necking zones width would be decreased. Hence, we argue that these simple models likely capture the first-order processes of lithospheric necking and the associated formation of necking zones observed at passive margins.

5. Conclusion

We performed two-dimensional thermo-mechanical numerical simulations of lithosphere extension without using strain softening/weakening mechanisms to quantify lithospheric necking. For a lithosphere in which the brittle-plastic upper crust is mechanically decoupled from the brittle-plastic upper mantle by a weak ductile lower crust, the evolution of crustal and mantle thinning is different but three stages can be consistently identified at the rift center: (1) a phase of widely distributed deformation within the crust and mantle characterized by moderate crustal thinning (stretching phase); (2) a phase of upper mantle necking associated with extreme slowing down of crustal thinning, and sometimes even crustal thickening caused by ductile flow in the weak lower crust towards the necking region; and (3) a phase of intense crustal thinning associated with the necking of the crust following the loss of strength of the upper mantle and its flexural rebound. In other words, the characteristic feature of our simulations with mechanically decoupled crust and mantle is

the depth-dependent and asynchronous necking of the lithosphere, where upper mantle lithosphere necks first and the upper crust necks subsequently. In contrast, in mechanically coupled models where the crust is entirely brittle-plastic, the crust and upper mantle lithosphere neck as one layer and only two stages of thinning can be recognized: (1) a stretching phase comparable to that of decoupled models and (2) a phase of intense crustal and upper mantle thinning, which reflects the necking of the brittle-plastic upper region of the lithosphere as an effective single layer.

In mechanically decoupled models, regions of relatively thickened continental crust (termed *continental lumps*) form on one or both sides of the rift center. These continental lumps are not formed in coupled models. The modeled lumps may explain observations of locally thick/unthinned continental crust at rifted margins, for example, the Galicia, Rockall, Hatton, and Porcupine Banks in the North Atlantic or the Briançonnais domain in the fossil Alpine Tethys margin.

The range of widths of the modeled necking zones weakly depends on the applied boundary conditions (constant extension velocity versus constant bulk extension rate) and on the applied mechanical crust-mantle coupling (coupled or decoupled). However, the applied boundary conditions have a significant impact on the necking dynamics: For constant bulk extension rates, wider models employ larger extension velocities at the boundaries. Once necking starts, these larger extension velocities apply essentially at the sides of the necking zones and larger extension velocities cause higher strain rates and more intense localization in the necking zones. This strain rate focussing effect is not present in models employing constant extension velocities.

The range of widths of the modeled necking zones is similar to the that of necking zones observed at natural rift systems, although the modeled widths are in average slightly larger than the observed widths. The similarity of modeled and natural widths of necking zones suggests that the applied 2-D thermo-mechanical models capture the first-order processes of lithospheric necking and the associated formation of necking domains.

Appendix A

A1. About the Nonuse of Strain Softening

In combination with a plastic yield function, many numerical models of lithospheric extension have employed strain softening, that is, the cohesion and/or friction angle is decreased with progressive plastic strain. We do not employ such strain softening here due to three reasons: First, strain softening makes the numerical results mesh sensitive and the numerical solutions do not converge to a correct numerical result with increasing mesh resolution (e.g., Sluys & De Borst, 1992). A possibility to avoid such mesh sensitivity is to apply a regularization method in which the characteristic thickness of shear zones is predefined a priori (e.g., Bažant & Jirásek, 2002). Such regularization avoids mesh sensitivity, but the shear zone thickness and, hence, the associated strain rates and stresses are not the self-consistent results of a thermo-mechanical process but are predefined. Second, strain softening algorithms require a number of input parameters such as (i) the amount of plastic strain before softening starts, (ii) the range of plastic strain in which softening occurs, or (iii) the value of cohesion and/or friction angle after the softening. All these parameters are little, if at all, known for natural rock so that strain softening algorithms are difficult to constrain with laboratory results or field observations. Third, the deformation in models with strain softening is intrinsically unstable and always generates prominent and localized shear bands across the entire brittle-plastic layers (e.g., upper and lower crust) in which strain softening is applied. We, however, aim to investigate the intensity and evolution of continuous and distributed lithospheric necking.

A2. Estimating the Width of Necking Zones With Analytical Solutions for Necking

Extension of the lithosphere can generate a mechanical necking instability, which has been studied with analytical solutions based on stability theory (e.g., Fletcher & Hallet, 1983; Ricard & Froidevaux, 1986; Zuber et al., 1986). Necking is used here as a general term to refer to local thinning due to the mechanical instability of a competent layer under extension (e.g., Schmalholz & Mancktelow, 2016; Smith, 1977). Mechanical instability of necking means that small geometrical perturbations on the layer interface, for example, along the surface or the crust-mantle boundary, amplify with rates that are faster than the applied bulk extension rate so that the layer can locally thin faster as it would do under homogenous thinning during extension.

In the analytical solutions the amplification of geometrical perturbations is quantified with the ratio of the current amplitude to the initial amplitude, A/A_0, of a perturbation. Assuming that prerift, initial, geometrical perturbations of crustal thickness have an amplitude, A_0, on the order of 100 m and that within a necking zone

the crustal thickness is reduced from initially 30 km to 10 km requires a final amplitude at the top and bottom of the crust of ~10 km and hence an amplification, $A/A_0 = 10^5$. The amplification is controlled by a dimensionless amplification rate, α, which is the ratio of the rate of amplification of the perturbation to the rate of uniform bulk extension of the lithosphere. When $\alpha > 0$, then extension is unstable because small geometrical perturbations amplify with rates faster than the bulk extension rate. The amplification in the analytical necking solutions is related to the amplification rate and the bulk uniform extension, ε, by (e.g., Fletcher & Hallet, 1983)

$$\frac{A}{A_0} = exp(-[1+\alpha]\cdot\varepsilon) \tag{A1}$$

Fletcher and Hallet (1983) calculated the amplification rates from the two-dimensional force balance equations, for typical flow laws of lithospheric rocks and for typical geothermal gradients, and they showed that amplification rates are between 40 and 100. Solving the above equation (A1) for ε, using amplification rates between 40 and 100, provides bulk uniform extensions of ~30% ($\varepsilon = \ln(10^5)/39$) and 12% ($\varepsilon = \ln(10^5)/99$).

The analytical stability theory assumes that natural geometrical perturbations can have any wavelength. A main result of the stability theory is that the amplitudes of these wavelengths amplify with different amplification rates, that is, there is dispersion. The stability theory further shows that the amplification rates have one maximum corresponding to a specific wavelength, termed the dominant wavelength. The dominant wavelength and its associated amplification rate, α, depend on the applied flow law and the density different between crust and mantle lithosphere. Fletcher and Hallet (1983) show that the dominant wavelengths for lithospheric extension are between 25 and 123 km for a wide variety of flow laws. Applying the above calculated bulk extension values of 30% and 12% to the 25- to 123-km range of dominant wavelengths provides a corresponding range of "extended" wavelengths between 28 and 166 km. The necking zone of a passive margin corresponds to half the extended wavelength and hence ranges between 14 and 83 km. These values agree with the observed widths of necking zones of 20 and 100 km for passive margins worldwide.

Acknowledgments
This research was supported by ExxonMobil in the framework of the project CEIBA (Center of Excellence In Basin Analysis). S. Schmalholz was supported by the University of Lausanne. We thank John Naliboff and an anonymous reviewer for their constructive comments and suggestions. The list of the physical parameters used in the simulations is provided in Table 1 and the models design is summarized in Figure 2.

References

Bassi, G. (1991). Factors controlling the style of continental rifting: Insights from numerical modelling. *Earth and Planetary Science Letters*, *105*(4), 430–452. https://doi.org/10.1016/0012-821X(91)90183-I

Bažant, Z. P., & Jirásek, M. (2002). Nonlocal integral formulations of plasticity and damage: Survey of progress. *Journal of Engineering Mechanics*, *128*(11), 1119–1149. https://doi.org/10.1061/(ASCE)0733-9399(2002)128: 11(1119)

Braun, J., & Beaumont, C. (1989). A physical explanation of the relation between flank uplifts and the breakup unconformity at rifted continental margins. *Geology*, *17*(8), 760–764. https://doi.org/10.1130/0091-7613(1989)017<0760:APEOTR>2.3.CO

Brune, S., & Autin, J. (2013). The rift to break-up evolution of the Gulf of Aden: Insights from 3D numerical lithospheric-scale modelling. *Tectonophysics*, *607*, 65–79. https://doi.org/10.1016/j.tecto.2013.06.029

Brune, S., Heine, C., Pèrez-Gussinyè, M., & Sobolev, S. V. (2014). Rift migration explains continental margin asymmetry and crustal hyper-extension. *Nature Communications*, *5*, 4014. https://doi.org/10.1038/ncomms5014

Brune, S., Williams, S. E., Butterworth, N. P., & Müller, R. D. (2016). Abrupt plate accelerations shape rifted continental margins. *Nature*, *536*(7615), 201–204. https://doi.org/10.1038/nature18319

Buck, W. R. (1991). Modes of continental lithospheric extension. *Journal of Geophysical Research*, *96*, 20,161–20,178.

Chenin, P., & Beaumont, C. (2013). Influence of offset weak zones on the development of rift basins: Activation and abandonment during continental extension and breakup. *Journal of Geophysical Research*, *118*, 1698–1720. https://doi.org/10.1002/jgrb.50138

Chenin, P., Manatschal, G., Picazo, S., Müntener, O., Karner, G. D., Johnson, C., & Ulrich, M. (2017). Influence of the architecture of magma-poor hyperextended rifted margins on orogens produced by the closure of narrow versus wide oceans. *Geosphere*, *13*(2), 1–18. https://doi.org/10.1130/GES01363.1

Dabrowski, M., Krotkiewski, M., & Schmid, D. W. (2008). MILAMIN: MATLAB-based finite element method solver for large problems. *Geochemistry, Geophysics, Geosystems*, *9*, Q04030. https://doi.org/10.1029/2007GC001719

Duretz, T., Petri, B., Mohn, G., Schmalholz, S. M., Schenker, F. L., & Müntener, O. (2016). The importance of structural softening for the evolution and architecture of passive margins. *Scientific Reports*, *6*(38), 704. https://doi.org/10.1038/srep38704

Dyksterhuis, S., Rey, P., Muller, R. D., & Moresi, L. (2007). Effects of initial weakness on rift architecture. *Imaging, Mapping and Modelling Continental Lithosphere Extension and Breakup*, *282*, 443–455. https://doi.org/10.1144/Sp282.18

England, P. (1983). Constraints on extension of continental lithosphere. *Journal of Geophysical Research*, *88*(B2), 1145. https://doi.org/10.1029/JB088iB02p01145

Evans, B., & Goetze, C. (1979). The temperature variation of hardness of olivine and its implication for polycrystalline yield stress. *Journal of Geophysical Research*, *84*(B10), 5505–5524. https://doi.org/10.1029/JB084iB10p05505

Fletcher, R. C., & Hallet, B. (1983). Unstable extension of the lithosphere: A mechanical model for basin-and-range structure. *Journal of Geophysical Research*, *88*(B9), 7457–7466. https://doi.org/10.1029/JB088iB09p07457

Gernigon, L., Gaina, C., Olesen, O., Ball, P., Pèron-Pinvidic, G., & Yamasaki, T. (2012). The Norway Basin revisited: From continental breakup to spreading ridge extinction. *Marine and Petroleum Geology*, *35*, 1–19. https://doi.org/10.1016/j.marpetgeo.2012.02.015

Goetze, C., & Evans, B. (1979). Stress and temperature in the bending lithosphere as constrained by experimental rock mechanics. *Geophysical Journal of the Royal Astronomical Society*, *59*, 463–478.

Haupert, I., Manatschal, G., Decarlis, A., & Unternehr, P. (2016). Upper-plate magma-poor rifted margins: Stratigraphic architecture and structural evolution. *Marine and Petroleum Geology*, *69*, 241–261. https://doi.org/10.1016/j.marpetgeo.2015.10.020

Hirth, G., & Kohlstedt, D. (2003). Rheology of the upper mantle and the mantle wedge: A view from the experimentalists. In J. Eiler (Ed.), *Inside the subduction Factory* (Vol. 138, pp. 83–105). Washington, DC: American Geophysical Union. https://doi.org/10.1029/138GM06

Huismans, R. S., & Beaumont, C. (2007). Roles of lithospheric strain softening and heterogeneity in determining the geometry of rifts and continental margins. In G. D. Karner, G. Manatschal, & L. M. Pinhiero (Eds.), *Imaging, mapping and modelling continental lithosphere extension and breakup* (Vol. 282, pp. 107–134). Special Publications. London: Geological Society.

Huismans, R., & Beaumont, C. (2011). Depth-dependent extension, two-stage breakup and cratonic underplating at rifted margins. *Nature*, *473*(7345), 74–78. https://doi.org/10.1038/nature09988

Huismans, R. S., Podladchikov, Y. Y., & Cloetingh, S. A. P. L. (2001). Transition from passive to active rifting: Relative importance of asthenospheric doming and passive extension of the lithosphere. *Journal of Geophysical Research*, *106*(B6), 11,271–11,291.

Jammes, S., & Lavier, L. L. (2016). The effect of bimineralic composition on extensional processes at lithospheric scale. *Geochemistry, Geophysics, Geosystems*, *17*, 3375–3392. https://doi.org/10.1002/2016GC006399

Lavier, L. L., & Manatschal, G. (2006). A mechanism to thin the continental lithosphere at magma-poor margins. *Nature*, *440*(7082), 324–328. https://doi.org/10.1038/nature04608

Lemiale, V., Muhlhaus, H. B., Moresi, L., & Stafford, J. (2008). Shear banding analysis of plastic models formulated for incompressible viscous flows. *Physics of the Earth and Planetary Interiors*, *171*, 177–186. https://doi.org/10.1016/j.pepi.2008.07.038

Manatschal, G., Muntener, O., Lavier, L. L., Minshull, T. a., & Peron-Pinvidic, G. (2007). Observations from the Alpine Tethys and Iberia-Newfoundland margins pertinent to the interpretation of continental breakup. *Geological Society Special Publication*, *282*(1), 291–324. https://doi.org/10.1144/SP282.14

Molnar, P., & Jones, C. H. (2004). A test of laboratoty based rheological parameters of olivine from an analysis of late Cenozoic convective removal of mantle lithosphere beneath the Sierra Nevada, California, USA. *Geophysical Journal International*, *156*, 555–564.

Müller, R. D., Gaina, C., Roest, W. R., & Hansen, D. L. (2001). A recipe for microcontinent formation. *Geology*, *29*(3), 203–206. https://doi.org/10.1130/0091-7613(2001)029<0203:ARFMF>2.0.CO;2

Naliboff, J., & Buiter, S. J. (2015). Rift reactivation and migration during multiphase extension. *Earth and Planetary Science Letters*, *421*, 58–67. https://doi.org/10.1016/j.epsl.2015.03.050

Nirrengarten, M., Manatschal, G., Yan, X., Kusznir, N., & Millot, B. (2016). Application of the critical Coulomb wedge theory to hyper-extended, magma-poor rifted margins. *Earth and Planetary Science Letters* (Vol. 442, pp. 121–132). United States: Elsevier B.V. https://doi.org/10.1016/j.epsl.2016.03.004

Pèrez-Gussinyè, M., & Reston, T. J. (2001). Rheological evolution during extension at nonvolcanic rifted margins: Onset of serpentinization and development of detachments leading to continental breakup. *Journal of Geophysical Research*, *106*(B3), 3961–3975. https://doi.org/10.1029/2000JB900325

Pèron-Pinvidic, G., & Manatschal, G. (2010). From microcontinents to extensional allochthons: Witnesses of how continents rift and break apart? *Petroleum Geoscience*, *16*(3), 189–197. https://doi.org/10.1144/1354-079309-903

Ricard, Y., & Froidevaux, C. (1986). Stretching instabilities and lithospheric boudinage. *Journal of Geophysical Research*, *91*(B8), 8314. https://doi.org/10.1029/JB091iB08p08314

Rosenbaum, G., Regenauer-Lieb, K., & Weinberg, R. F. (2010). Interaction between mantle and crustal detachments: A nonlinear system controlling lithospheric extension. *Journal of Geophysical Research*, *115*, B11412. https://doi.org/10.1029/2009JB006696

Rybacki, E., & Dresen, G. (2004). Deformation mechanism maps for feldspar rocks. *Tectonophysics*, *382*(3–4), 173–187. https://doi.org/10.1016/j.tecto.2004.01.006

Schmalholz, S. M. (2011). A simple analytical solution for slab detachment. *Earth and Planetary Science Letters*, *304*(1–2), 45–54. https://doi.org/10.1016/J.EPSL.2011.01.011

Schmalholz, S. M., Duretz, T., Schenker, F. L., & Podladchikov, Y. Y. (2014). Kinematics and dynamics of tectonic nappes: 2-D numerical modelling and implications for high and ultra-high pressure tectonism in the western alps. *Tectonophysics*, *631*, 160–175.

Schmalholz, S. M., & Fletcher, R. C. (2011). The exponential flow law applied to necking and folding of a ductile layer. *Geophysical Journal International*, *184*, 83–89. https://doi.org/10.1111/j.1365-246X.2010.04846.x

Schmalholz, S. M., & Mancktelow, N. S. (2016). Folding and necking across the scales: a review of theoretical and experimental results and their applications. *Solid Earth*, *7*(5), 1417–1465. https://doi.org/10.5194/se-7-1417-2016

Schmalholz, S. M., Podladchikov, Y. Y., & Schmid, D. W. (2001). A spectral/finite difference method for simulating large deformations of heterogeneous, viscoelastic materials. *Geophysical Journal International*, *145*, 199–208.

Schmalholz, S. M., Schmid, D. W., & Fletcher, R. C. (2008). Evolution of pinch-and-swell structures in a power-law layer. *Journal of Structural Geology*, *30*(5), 649–663. https://doi.org/10.1016/j.jsg.2008.01.002

Shewchuk, J. R. (2002). Delaunay refinement algorithms for triangular mesh generation. *Computational Geometry-Theory and Applications*, *22*, 21–74. https://doi.org/10.1016/s0925-7721(01)00047-5

Sluys, L. J., & De Borst, R. (1992). Wave propagation and localization in a rate-dependent cracked medium—Model formulation and one-dimensional examples. *International Journal of Solids and Structures*, *29*(23), 2945–2958. https://doi.org/10.1016/0020-7683(92)90151-I

Smith, R. B. (1977). Formation of folds, boudinage, and mullions in non-Newtonian materials. *Bulletin of the Geological Society of America*, *88*, 312–320. https://doi.org/10.1130/0016-7606(1977)88<312:FOFBAM>2.0.CO;2

Sutra, E., Manatschal, G., Mohn, G., & Unternehr, P. (2013). Quantification and restoration of extensional deformation along the Western Iberia and Newfoundland rifted margins. *Geochemistry, Geophysics, Geosystems*, *14*, 2575–2597. https://doi.org/10.1002/ggge.20135

Vink, G. E., Morgan, W. J., & Zhao, W.-L. (1984). Preferential rifting of continents: A source of displaced terranes. *Journal of Geophysical Research*, *89*(B12), 10,072–10,076. https://doi.org/10.1029/JB089iB12p10072

Weissel, J. K., & Karner, G. D. (1989). Flexural uplift of rift flanks due to mechanical unloading of the lithosphere during extension. *Journal of Geophysical Research*, *94*(B10), 13,919–13,950.

Wilks, K. R., & Carter, N. L. (1990). Rheology of some continental lower crustal rocks. *Tectonophysics*, *182*(1-2), 57–77. https://doi.org/10.1016/0040-1951(90)90342-6

Zuber, M. T., Parmentier, E. M., & Fletcher, R. C. (1986). Extension of continental lithosphere—A model for two scales of basin and range deformation. *Journal of Geophysical Research*, *91*(B5), 4826–4838. https://doi.org/10.1029/JB091iB05p04826